JOURNAL OF THERMOPHYSICS AND HEAT TRANSFER
Vol. 25, No. 1, January–March 2011

Numerical Simulation of Liquid Rocket Engine Thrust Chamber Regenerative Cooling

Yu-Dong Kang* and Bing Sun†
Beijing University of Aeronautics and Astronautics, 100191 Beijing, People's Republic of China

DOI: 10.2514/1.47701

The objective of this paper is to develop and compare multidisciplinary, multidimensional, numerical methodologies to predict the hot-gas-side and coolant-side heat transfer in regeneratively-cooled rocket engine thrust chamber. The first methodology used empirical equations to simulate the hot-gas convective and radiative heat transfer; the second methodology used computational fluid dynamics to simulate the hot-gas convective and radiative heat transfer; heat transfer in the coolant and in the cooling channel was solved in a conjugate manner for the two methodologies. Systematic parametric studies on effects of combustion chemistry, radiation coupling, and grid refinement were performed and assessed. The methodologies were assessed by existing data from Arnold Engineering Development Center high-enthalpy nozzle tests and hot-firing test of a LO_2-LH_2 thrust chamber. Results indicate that the second methodology with finite-rate chemistry employed in this study can be an effective method for predicting the flow and heat transfer in regeneratively-cooled thrust chamber, but needs further modifications.

Nomenclature

A	=	cross-sectional area
a	=	absorption coefficient
C_p	=	heat capacity
C_μ	=	turbulence-modeling constants
D	=	diffusivity, diameter
D_{ij}	=	Reynolds stress model diffusion term
E	=	total energy, empirical constant
h	=	enthalpy, heat transfer coefficient
I	=	is radiation intensity
$\mathbf{J}_j$	=	diffusion flux of species
n	=	refractive index
P_{ij}	=	Reynolds stress model stress production term
Pr	=	Prandtl number
R	=	recovery factor
$\mathbf{r}$	=	position vector
$\mathbf{s}$	=	direction vector
s	=	path length
$\mathbf{s}'$	=	scattering direction vector
T	=	temperature
u, v, w	=	mean velocities in three directions
x	=	Cartesian coordinates
Y	=	species concentration
y^+	=	dimensionless distance to the wall
ε	=	emissivity coefficient
ε_{ij}	=	Reynolds stress model dissipation term
η_c	=	combustion efficiency
κ	=	turbulent kinetic energy
$\boldsymbol{\lambda}$	=	thermal conductivity
μ	=	viscosity
ρ	=	density
σ	=	Stefan–Boltzmann constant
σ_s	=	scattering coefficient
$(\tau_{ij})_{\text{eff}}$	=	deviatoric stress tensor
Φ	=	phase function
Φ_{ij}	=	Reynolds stress model pressure-strain redistribution term
Ω'	=	solid angle
ω	=	chemical-species production rate

Subscripts

c	=	convective, chamber
P	=	cell adjacent to wall
r	=	radiative, recovery
t	=	turbulent flow, throat
w	=	wall
wg	=	hot-gas-side wall

I. Introduction

IN ORDER to optimize combustion process and ensure integrity of thrust chamber there is a need to perform a comprehensive thermal analysis, it is especially important for the design of reusable engines. Adequate understanding and accurate prediction of heat transfer characteristics, heat pickup, and wall temperature in the thrust chamber is prerequisite for reusable design. The continuous demand for the higher performance engines has resulted in higher pressure and temperature for the thrust chambers and the need for more sophisticated cooling methods, such as regenerative cooling [1,2]. Thermal analysis of rocket engines is a coupled heat transfer problem of hot gas, chamber wall and the coolant.

The traditional method of evaluating those characteristics in thrust chamber was mainly based on one-dimensional analysis with Nusselt-type empirical equations [3–5]. Such traditional methods require some tuning parameters to realize consistent heat load and pressure drop with experimental data. Computational fluid dynamics (CFD) technique was considered to be an effective approach to improve the traditional thrust chamber design and evaluation. There were some CFD studies about the heat transfer characteristics in thrust chamber. Wang and Luong [6] developed a multidisciplinary computational methodology which incorporated an axisymmetric CFD for the hot-gas thermal environment, three-dimensional heat conduction model for the liner and one-dimensional hydraulic model for the coolant channel to predict the hot-gas-side and coolant-side heat transfer in film cooling assisted, regeneratively-cooled liquid rocket engine combustors, the predicted wall heat flux compared well with that measured from a 40 k calorimeter thrust chamber. Liu et al. [7] conducted a fully coupled multidisciplinary CFD simulation with heat conduction computation model and quasi-one-dimensional

Received 18 October 2009; revision received 10 August 2010; accepted for publication 15 August 2010.

*Ph.D. Candidate, School of Astronautics; kyd@sa.buaa.edu.cn.
†Professor, School of Astronautics.

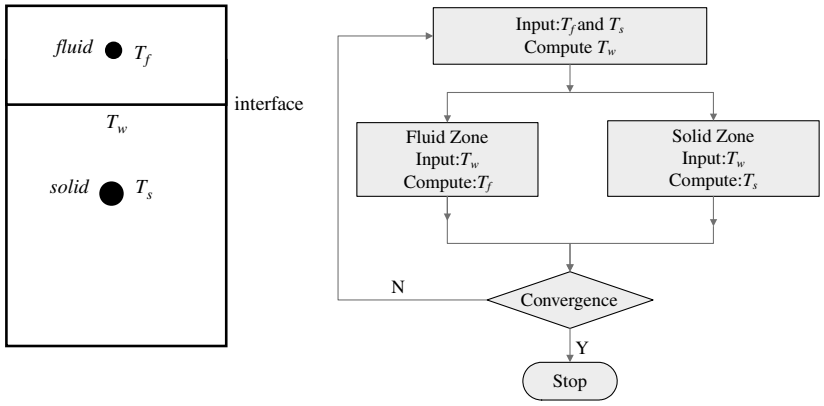

a) Schematic **b) Procedure**

Fig. 1 Schematic and procedure of conjugate heat transfer.

water cooling channel model for a water-cooled thruster nozzle, the calculated temperatures at cooling channel outlet compared favorably with experimental data. Naraghi et al. [8] developed a model with conjugating two proven rocket thermal analysis codes, TDK and RTE, via an interface file to design and analyze of regeneratively-cooled rocket engine, the accuracy of that model was examined by comparing its results to those of other methods. Naraghi and Jokhakar [9] presented a computational methodology for thermal analysis of hot-gas-side and coolant-side of regeneratively-cooled liquid rocket engines, their model was composed of an axisymmetric CFD model for the hot-gas-side flow and RTE for the coolant flow and wall conduction, the integrated CFD-RTE model was validated by comparing its results with the published data. In high aspect ratio cooling channels the flow exhibits strongly three-dimensional features, in [6–9] studies, they neglected three-dimensional combustion and coolant flowfield and had not considered the flames from injector elements. Negishi et al. [10,11] carried out subscale thrust chamber heat transfer simulations considering atomization process with discrete phase model and hydrogen–oxygen finite-rate chemical reactions using hot-gas-side wall temperature distribution evaluated from experimental results, the computed hot-gas-side wall heat flux showed good agreement with that from experiment, in their studies, the hot gas, chamber wall, coolant heat transfer were decoupled and paid no attention to radiation heat transfer.

The main objective of this study is to propose two computational methodologies for regenerative cooling coupled flow and heat transfer analysis. The difference of the two methodologies was the mode to simulate the hot-gas convective and radiative heat transfer. The first methodology used empirical equations, while the second methodology used CFD. Heat transfer in the coolant and in the cooling channel was solved in a conjugate manner for the two methodologies. For the second methodology, the hydrogen-oxygen finite-rate chemical reaction were evaluated by eddy dissipation concept (EDC) model for nonequilibrium hot-gas flow, radiative heat transfer was solved with discrete ordinates (DO) model. In this study, numerical simulations have been performed using the FLUENT solver. Both methodologies were performed and assessed by existing data from Arnold Engineering Development Center (AEDC) high-enthalpy nozzle tests which recorded bulk temperature rise and hot-firing test of a LO_2-LH_2 thrust chamber which recorded coolant pressure drop and bulk temperature rise.

II. Computational Methodology

A. System of Governing Equations

The equations governing the coolant flow are the continuity, momentum, and energy equations:

$$\frac{\partial}{\partial x_j}(\rho u_j) = 0 \tag{1}$$

$$\frac{\partial}{\partial x_j}(\rho u_j u_i) = -\frac{\partial p}{\partial x_i} + \frac{\partial \tau_{ij}}{\partial x_j} \tag{2}$$

$$\frac{\partial}{\partial x_i}(u_i(\rho E + p)) = \frac{\partial}{\partial x_j}\left[\left(\lambda + \frac{c_p \mu_t}{P\Delta_t}\right)\frac{\partial T}{\partial x_j} + u_i(\tau_{ij})_{\text{eff}}\right] + S_h \tag{3}$$

The equations governing the hot-gas flow are the continuity equation as Eq. (1), momentum equation as Eq. (2), species continuity equation as Eq. (4), and energy equation as Eq. (5):

$$\frac{\partial}{\partial x_j}(\rho u_j Y_j) = \frac{\partial}{\partial x_j}\left[\left(\rho D + \frac{\mu_t}{Sc_t}\right)\frac{\partial Y_i}{\partial x_j}\right] + \omega_i \tag{4}$$

$$\frac{\partial}{\partial x_i}(u_i(\rho E + p)) = \frac{\partial}{\partial x_j}\left[\left(\lambda + \frac{c_p \mu_t}{P\Delta_t}\right)\frac{\partial T}{\partial x_j} - \sum_j h_j \mathbf{J}_j + u_i(\tau_{ij})_{\text{eff}}\right] + S_h \tag{5}$$

The shear stress τ_{ij} in the preceding equations can be expressed as

$$\tau_{ij} = (\mu + \mu_t)\left(\frac{\partial u_i}{\partial x_j} + \frac{\partial u_j}{\partial x_i} - \frac{2}{3}\frac{\partial u_k}{\partial x_k}\delta_{ij}\right) \tag{6}$$

The Reynolds stress model (RSM) was used to simulate the coolant and hot-gas turbulence. The RSM closes the Reynolds-averaged Navier–Stokes equations by solving transport equations for the Reynolds stresses, together with an equation for the dissipation rate:

$$\frac{\partial(\rho u_k \overline{u_i' u_j'})}{\partial x_k} = P_{ij} + \Phi_{ij} - \varepsilon_{ij} + D_{ij} \tag{7}$$

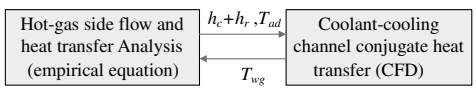

a) schematics of 1st methodology

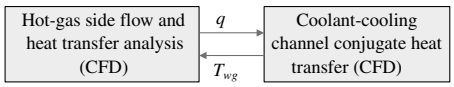

b) schematics of 2nd methodology

Fig. 2 Schematic of first and second methodology procedure.

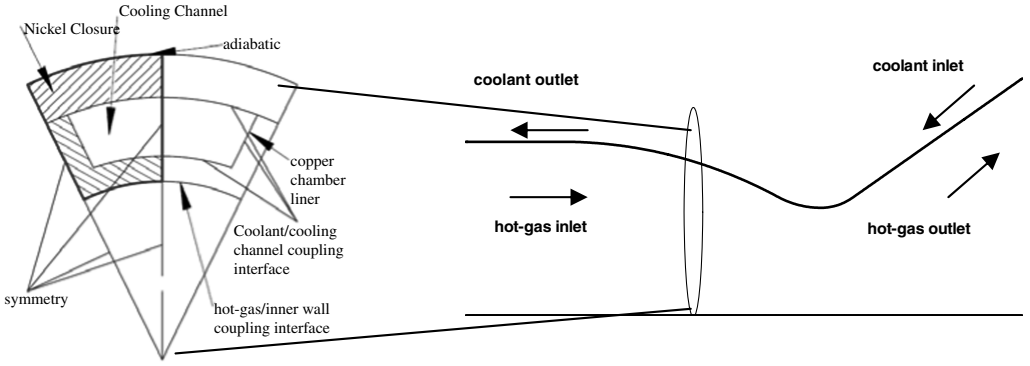

Fig. 3 Schematics of regenerative cooling thrust chamber and boundary condition at a typical cross section.

For the cooling channel, the heat conduction is governed by

$$\frac{\partial}{\partial x_j}\left(\lambda \frac{\partial T}{\partial x_j}\right) = 0 \tag{8}$$

In the hot-gas flow region, numerical simulations were carried out using the density-based solver, while the pressure-based solver was used in the coolant flow region numerical simulations and SIMPLE was used as the pressure-velocity coupling method. The convective terms were evaluated by the second order upwind, viscous terms were evaluated by the central differencing.

Both six-species, nine-reaction and six-species, seven-reaction reduced reaction mechanism [12] were used to describe the finite-rate, hydrogen/oxygen afterburning chemical kinetics, the EDC model was used to include detailed chemical reaction mechanisms in turbulent flow. The six-species are H_2, O_2, H_2O, H, O and OH.

A modified standard wall function approach, which can consider the wall roughness effect on flow and heat transfer was employed to provide wall boundary-layer solutions that are less sensitive to the near-wall grid spacing. The convective heat transfer using modified standard wall function approach can be calculated as

$$q_c = \frac{(T_w - T_P)\rho c_p C_\mu^{1/4} k_P^{1/2}}{T^*} \tag{9}$$

Where T^* is the nondimensional temperature.

The radiative heat transfer is analyzed by solving the radiative transfer equation (RTE):

$$\nabla \cdot (I(\mathbf{r},\mathbf{s})\mathbf{s}) + (a+\sigma_s)I(\mathbf{r},\mathbf{s}) = an^2\frac{\sigma T^4}{\pi} + \frac{\sigma_s}{4\pi}\int_0^{4\pi} I(\mathbf{r},\mathbf{s})\Phi(\mathbf{s},\mathbf{s}')\,\mathrm{d}\Omega' \tag{10}$$

Discrete-ordinate method was used to solve the RTE, and H_2O is the major radiating medium. The total emissivity and absorptivity of H_2O was calculated by the method supplied by [13].

B. Empirical Method

For the empirical method, the third kind of thermal boundary conditions with heat transfer coefficient and recovery temperature were imposed at the hot-gas-side wall. Heat transfer coefficient combines convective and radiative heat transfer coefficient, recovery temperature takes into account imperfect combustion as well as incomplete heat recovery and was defined as

$$T_r = T_g + R(T_{\mathrm{ran}}\eta_c^2 - T_g) \tag{11}$$

Hereby the recovery factor R is an empirical value depending on the gas Prandtl number on the boundary-layer status.

The convective heat transfer from the hot gas to the hot-gas-side walls was calculated using Nusselt-type correlations. Two approaches for the tube flow model were considered: a) the Bartz equation [14]

$$h_c = \frac{0.026}{D_t^{0.2}}\left(\frac{\mu^{0.2}c_p}{P\Delta^{0.6}}\right)_0\left(\frac{p_c}{c^*}\right)^{0.8}\left(\frac{A_t}{A}\right)^{0.9}\sigma \tag{12}$$

and b) the Cinjarew equation [15]

$$h_c = 0.01975\frac{\lambda^{0.18}\cdot(\dot{m}c_p)^{0.82}}{D_h^{1.82}}\left(\frac{T_r}{T_{wg}}\right)^{0.35} \tag{13}$$

Values of viscosity, specific heat and conductivity are computed at a mean temperature $T = (T_r + T_{wg})/2$.

Radiative heat transfer coefficient can be defined in the following way [16]:

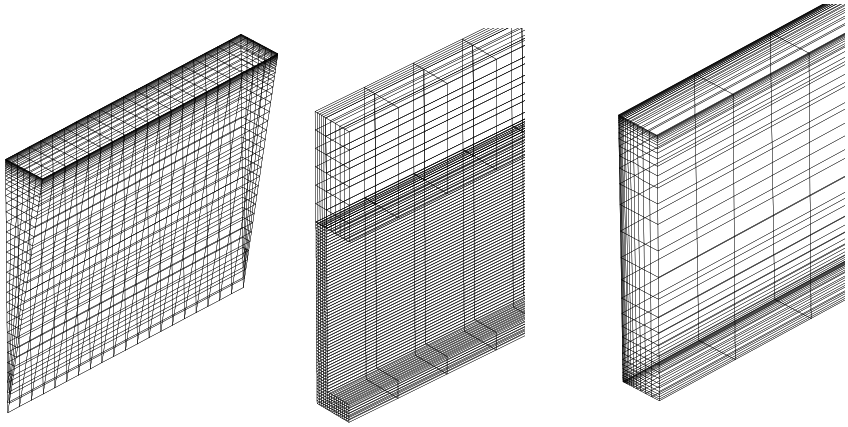

a) Hot-gas flow region **b) Cooling channel** **c) Coolant flow region**

Fig. 4 Layout of numerical gird (close-up at the cylinder part of thrust chamber).

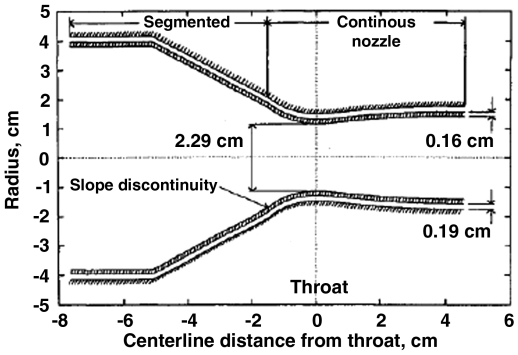

Fig. 5 AEDC nozzle geometry.

$$h_r = \frac{(1+\varepsilon_w)\times 5.67 \times [\alpha(T_g)^4 - \alpha_g(T_{wg})^4]}{2\times 10^8 \times (T_r - T_{wg})} \tag{14}$$

C. Numerical Method

The heat transfer in regenerative cooling thrust chamber under operating conditions involves a) heat transfer from the hot gas to inner wall, b) heat conduction through chamber wall, and c) convective heat transfer from chamber wall to coolant. To accurately predict the temperature in the cooling channel, particularly on the hot-gas-side wall, one needs to simultaneously compute all three domains, but such a procedure can be unstable. In the present study, we solve the coolant flow field along with heat transfer in the cooling channel in a conjugate manner, while the temperature and wall flux exchange between hot gas and inner wall was controlled by UDF, in such a way, we can couple the flow and heat transfer in all three domains.

For conjugate heat transfer, the coupling of fluid and solid domains is accomplished through a common interface temperature T_w which ensures the balance of heat flux at interface, as shown in Fig. 1a and Eq. (16), the fluid zone is on the top and the solid zone is on the bottom in this figure. The algorithm for performing conjugated heat transfer is shown in Fig. 1b. Firstly, compute the wall temperature along the solid-fluid interface by setting the heat flux for the fluid face equal to that for solid face as Eq. (16). Secondly, solve the fluid zone/solid zone using the computed interface temperature as boundary condition, new fluid/solid temperature at adjacent grids of interface can be obtained. From the fluid and solid temperature computed at adjacent grids of interface, a new interface temperature distribution can be obtained through Eq. (16). This completes one iteration cycle, the solver solves both the fluid and solid domains and updates the temperature at interface at each iteration. This algorithm proceeds iteratively until the convergence is achieved:

Table 1 AEDC nozzle run conditions

	Run 1	Run 2	Run 3	Run 4
$P_{\text{o, air}}$, atm	126.5	137.0	104.4	94.3
$T_{\text{o, air}}$, K	5000	5240	4600	5100
M_{water}, kg/s	5.234	5.234	3.216	3.204
T_{inlet}, K	309	307	289	289

Table 2 AEDC nozzle grid distribution

Domain	Number of nodes
Air flow	
Segment 1	$47 \times 45 \times 7$
Segment 2	$51 \times 27 \times 7$
Solid	
Segment 1	$47 \times 9 \times 7$
Segment 2	$51 \times 9 \times 7$
Water flow	
Segment 1	$47 \times 18 \times 11$
Segment 2	$51 \times 18 \times 11$

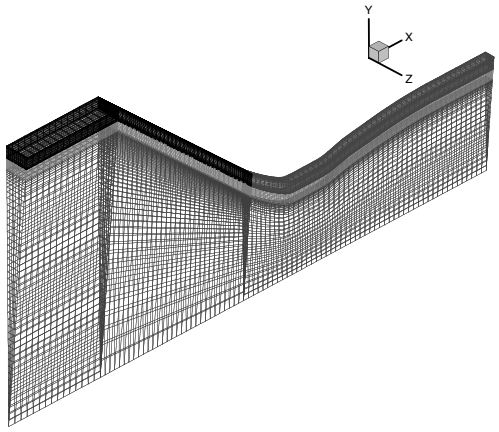

Fig. 6 AEDC nozzle grid layout.

$$T_{fw} = T_{sw} = T_w \tag{15}$$

$$k_f \left.\frac{\partial T}{\partial n}\right|_{\text{fluid}} = k_s \left.\frac{\partial T}{\partial n}\right|_{\text{solid}} \tag{16}$$

Figure 2 shows the schematic of first and second methodology numerical procedure. For the first methodology, the total heat transfer coefficient $h_c + h_r$ and recovery temperature T_r were imposed at the hot-gas-side wall, simultaneously compute the cooling channel heat conduction and coolant flow. For the second methodology, an initial hot-gas-side wall temperature distribution was assumed to start the calculation of the hot-gas flow region governing equations until convergence, then the hot-gas-side wall heat flux distribution can be obtained and used as the boundary condition for cooling channel/coolant conjugate heat transfer, after the calculation was converged, a new hot-gas-side wall temperature distribution was obtained. The iteration proceeded until the hot-gas-side wall heat flux and temperature became almost unchanged.

For the first methodology, the empirical equations were imposed at hot-gas-side walls via user defined functions (UDF). For the second methodology, hot-gas/inner wall common boundary data exchange was controlled by UDF. The hydrogen thermophysical properties were implemented in the solver via UDF.

III. Computational-Grid Generation and Boundary Conditions

The chamber wall is cooled by hydrogen flowing in the opposite direction to the hot gas flow. There are 300 milled axial coolant channels that are closed out by an electroforming precess which deposits a copper barrier, followed by a nickel closeout over the coolant channels. Because of the axisymmetric configuration of the thrust chamber, the simulation was carried out only for 0.6 ° in the circumferential direction assuming the symmetry condition at the circumferential boundaries.

Figure 3 shows the boundary condition scheme of the two methodologies. Fixed total conditions were used at the inlet of the thrust chamber, the total pressure was 10.2 MPa, total temperature was 3605 K, and total mass flow rate was 156 kg/s. The mass fractions of H2, O2, H, O, OH, and H2O are 0.0287, 0.0164, 0.0024, 0.0061, 0.0687, and 0.8778; each chemical species at thruster was calculated by the one-dimensional chemical equilibrium calculation program CEA [17]. At the coolant inlet boundary, static pressure was 15.9 MPa, static temperature was 35 K, and mass flow rate was 20.81 kg/s. No-slip boundary condition was specified for the thrust walls, coupling walls surface roughness was specified as 3.2 μm (typical value obtained during manufacturing of the channels).

Figure 4 shows the grid scheme of the two methodologies. nonconformal grid system was employed, hexahedral/tetrahedral mesh was used as grid topology in hot-gas region, hexahedral mesh

Table 3 Measured and computed water temperature rise of the second segment

Run number	Experimental coolant temperature rise	Numerical coolant temperature rise		Percent error	
		Frozen flow	Nonequilibrium flow	Frozen flow	Nonequilibrium flow
1	13.9 K	12.3 K	14.5 K	−11.5%	4.3%
2	15.0 K	13.5 K	16.1 K	−10%	7.3%
3	18.9 K	15.5 K	17.5 K	−17.9%	−7.4%
4	20.0 K	15.7 K	18.5 K	−21.5%	−7.5%

was used as grid topology in chamber wall and coolant region. For a good resolution of the boundary layer that develops along coupling interface, the grids were clustered in the vicinity of coupling interface with wall y^+ between 30 and 300, as shown in Fig. 4. These computational grids were generated using the software package GAMBIT. For the first methodology, the cooling channel and coolant grid were adopted. For the second methodology, the hot gas, cooling channel and coolant grid were adopted. The hot-gas, inner wall, rib, nickel closet, and coolant were discretized with nodes distribution in axial × radial × circumferential directions as $255 \times 50 \times 7$, $255 \times 5 \times 10$, $255 \times 38 \times 4$, $255 \times 5 \times 7$, and $255 \times 33 \times 15$, respectively.

IV. AEDC High-Enthalpy Nozzle Verification

The water-cooled high-enthalpy, supersonic wind nozzle analyzed by Shope [18] has been simulated using the second numerical scheme, it has been used as a verification in [19,20]. The nozzle configuration is shown in Fig. 5. The run conditions implemented in the simulation are provided in Table 1, and provide direct comparison to experiment. Water inlet pressure was 68 atm for each run. When assume nonequilibrium flow, the arc-heated air is modeled here as nonvitiated, five-specie reacting air (O_2, NO, O, N, N_2) using the chemical kinetic provided by [21]. The initial conditions are assumed to be in chemical equilibrium, and the specie concentrations are predicted using chemical equilibrium calculation program.

The domain is a 5-deg azimuthal slice of the nozzle, includes air flow region, solid and water flow region. Standard wall function was used to bridge the viscosity-affected region between the wall and the fully-turbulent region, RSM turbulence model was used to model the turbulent air and water flow. Table 2 documents the grid distribution for various regions of the nozzle, resulting in y^+ values for the first cell off wall ranging from 30 to 300. The grids/domains are shown in Fig. 6.

Predicted coolant bulk temperature rise is listed in Table 3. In each run, the predicted coolant bulk temperature rise using nonequilibrium arc-heated air is within ±8% of the experimentally measured values. This is excellent agreement considering the complex fluid-thermal physics involved and ±7% of experimental data uncertainty. The predicted coolant bulk temperature rise using frozen flow is lower than experimentally measured values, and the maximum error exceeds 20%.

Figure 7 shows the results comparison obtained by present method with references, it can be seen from the figure that the present method provide higher heat flux and temperature. Figure 8 illustrates the typical oxygen recombination effects taking place within the nozzle flow. Near the hot-gas-side wall the air tends to recombine, causing substantial increase in O_2 mass fraction. We conclude that the second methodology considering finite-rate chemistry can be potentially be used as a general predictive tool for numerical simulation of regeneratively-cooled thrust chamber flow and heat transfer.

V. Results and Discussions

A. Thermophysical Properties of Supercritical Hydrogen

As the thermophysical properties of coolant are stored in the center of a control volume and there are large pressure drop and obvious stratification of the flow in cooling channel [22,23]. The density of supercritical hydrogen varies by more than an order of magnitude over the temperature range considered. Variations in the specific heat, viscosity and thermal conductivity are similarly quite strong. One of the important issues in the cooling channel is the effect of variable properties on the heat transfer and pressure drop characteristics of the channel. It is necessary to make the calculation of thermophysical properties in each control volume simple and in high accuracy. The density, specific heat, viscosity, and thermal conductivity were solved with the Redlich–Kwong equation of state (EOS), departure functions related to Peng–Robinson EOS, the Lucas method, and the TRAPP method, respectively.

Figure 9–12 represents the density, viscosity, thermal conductivity, specific heat capacity at constant pressure as a function of pressure and temperature, respectively. It can be seen from the figures that the density, viscosity, thermal conductivity agree well with National Institute of Standards and Technology (NIST) data [24] except the specific heat capacity at constant pressure, so in low

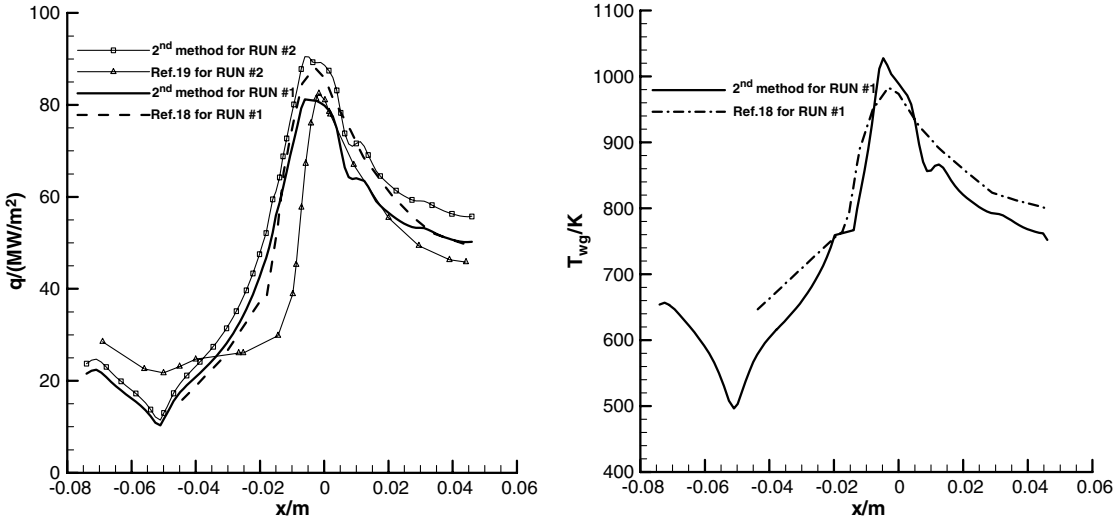

Fig. 7 Comparison of simulation results with refs: left, air-side heat flux distribution; right, air-side temperature distribution.

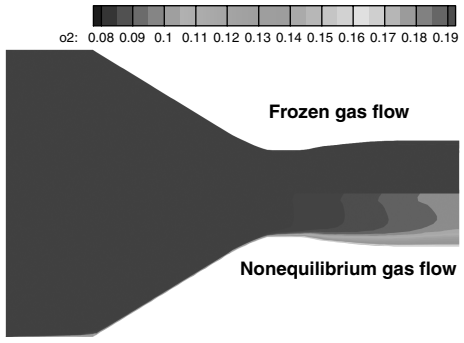

Fig. 8 Comparison of O_2 mass fraction contours for air flow.

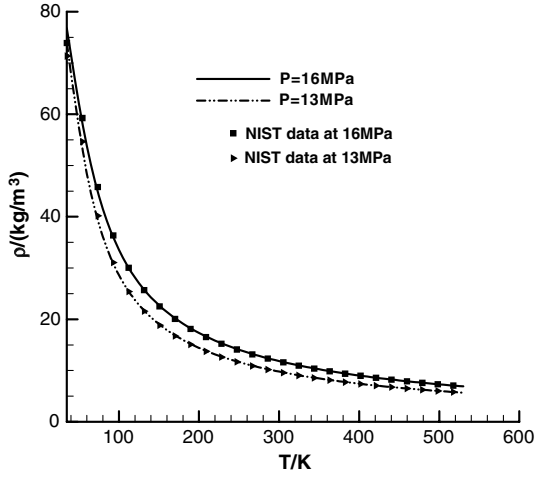

Fig. 9 H_2 density comparison.

temperature region ($T < 250$ K), the values of specific heat capacity at constant pressure are obtained by using a bilinear interpolation from a existing P-T table with the data from NIST database.

B. Grid Verification

Grid convergence analysis has been performed by comparison of the hot-gas-side wall heat flux and temperature obtained with the base grid, coarse gird and finer grid (Table 4). Figure 13 illustrates hot-gas-side wall heat flux and temperature. Both comparisons clearly demonstrate that the solutions with base and finer grids are close to each other and thus to the grid converged results, there are apparent solutions discrepancies between the coarse gird and the two finer grids. For the base and finer grids, the solutions with finer grid

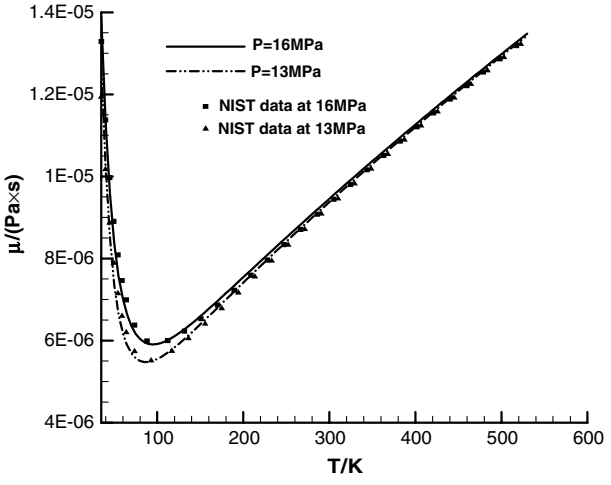

Fig. 10 H_2 viscosity comparison.

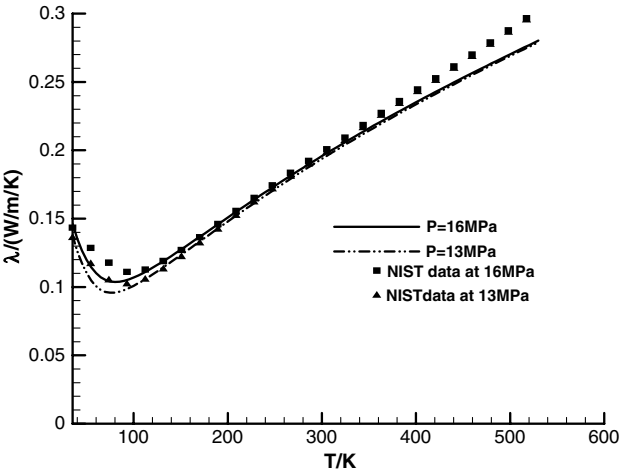

Fig. 11 H_2 thermal conductivity comparison.

are less than those with base grid, the biggest discrepancies have been noticed in convergent part of thrust chamber, the biggest difference between the two solutions is less than 2% for both the wall heat flux and temperature, which are shown in Fig. 13. The performed grid verification demonstrates that the base mesh distribution is suitable to accurately describe the regeneratively-cooled thrust chamber flow and heat transfer.

C. Numerical Simulation Results

The run matrix is shown in Table 5. These cases were built up systematically to understand modeling effects such as chemistry, radiation and methodology.

Figure 14 depicts the computed H_2O mass fraction, static temperature, static pressure contours for case 1 and case 3, respectively. It illustrates the typical H_2O recombination effects taking place within the thruster flow. The dissociated species tends to recombine near the hot-gas-side wall, causing substantial increase in H_2O mass fraction. The H_2O recombination also develops as the flow expands and cools through the thruster. In the combustion chamber and the convergent region of nozzle, the nonequilibrium effect is not so obvious for the low hot-gas velocity and high hot-gas temperature, while in the divergent region of nozzle, due to rapid gas expansion, the nonequilibrium effect is obvious, as Fig. 14 shows. For the formation of H_2O is an exothermic reaction, there is continuously heat release as the hot-gas flow in the thruster, so the computed temperature and pressure for case 1 are higher than those for case 3 at the same axial position. As shown in Fig. 14, temperatures and pressures are not uniform along the radial direction and are higher in the central region and lower close to the wall.

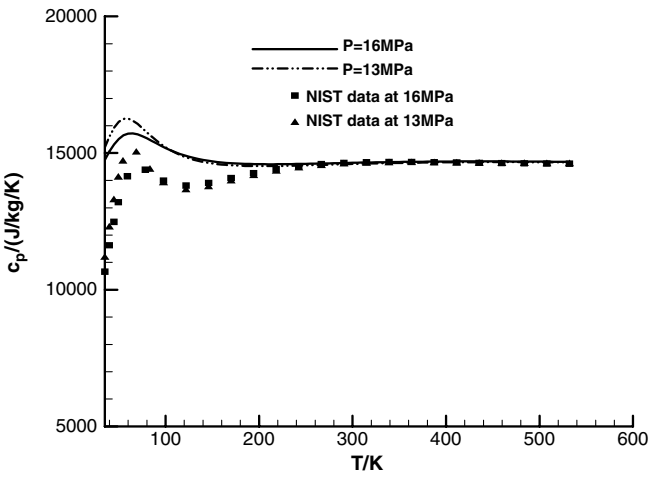

Fig. 12 H_2 specific heat capacity comparison.

Table 4 Number of various region nodes for grid verification

Grid	Hot gas	Inner wall	Rib	Nickel closet	Coolant
Coarse	175 × 50 × 3	175 × 5 × 10	175 × 38 × 4	175 × 5 × 7	175 × 33 × 15
Finer	255 × 70 × 5	255 × 7 × 16	255 × 57 × 6	255 × 7 × 11	255 × 41 × 17

Table 5 Run matrix

	Case 1	Case 2	Case 3	Case 4	Case 5 (Bartz)	Case 6 (Cinjarew)
Chemistry	on	on	off	off	off	off
Radiation	on	off	on	off	empirical	empirical

Figure 15 shows the computed radiative heat flux for case 1 and case 3. As expected, high radiative heating occurs inside the combustion chamber within which the high temperature and high H_2O concentration are prevalent. As the propulsive flow expands past the throat, the temperature drops, hence the radiative heat flux is low. In the divergent region of nozzle, although the hot-gas temperature is lower, the radiative heat flux increase for case 1. The reason for this is that the H_2O mass fraction increases for the obvious nonequilibrium effect of hot gas past the throat, much more H_2O participate in the radiation. Generally speaking, the radiative heat flux is only a small part of the total heat flux, which is reasonable for a LO_2-LH_2 rocket engine, but it should not be neglected.

Figure 16 shows the wall heat flux distribution using seven reaction and nine reaction. Both reaction belong to reduced reaction mechanism, which includes the basic species as well as the intermediate species OH, H, O. It shows that the deviations of the computed wall flux with both reduced reaction mechanism are very small.

Figure 17 shows the wall heat flux for all cases. The results show that the computed wall heat flux profile for case 1, 2, 3, 4 follow the same pattern and the maximum wall heat flux occurs upstream of the throat. For the formation of H_2O is an exothermic reaction, the nonequilibrium thermodynamic effect is to change the effective heat capacitance and mixture thermal conductivity near the wall, the wall heat flux assuming nonequilibrium flow (case 1, 2) is higher than using frozen flow (case 3, 4). The wall heat flux profile of case 5 follows the same pattern as case 6 and the maximum wall heat flux occurs downstream of the throat. The wall heat flux calculated by Cinjarew equation is higher than Bartz equation in the divergent part. As there is an arc with small radius downstream the throat, which causes rapid gas expansion after the arc and thus a subsequent

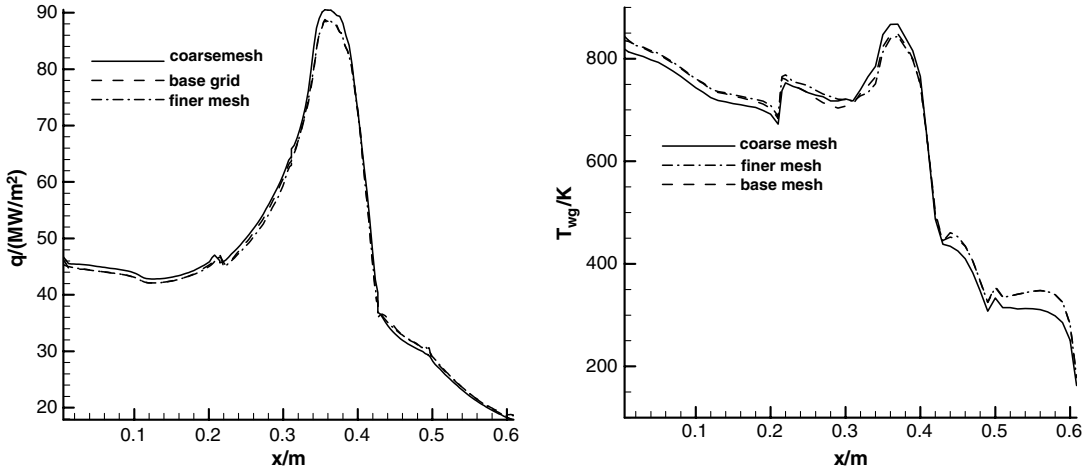

a) Hot-gas side total wall heat flux **b) Hot-gas side wall temperature**

Fig. 13 Grid verification plots.

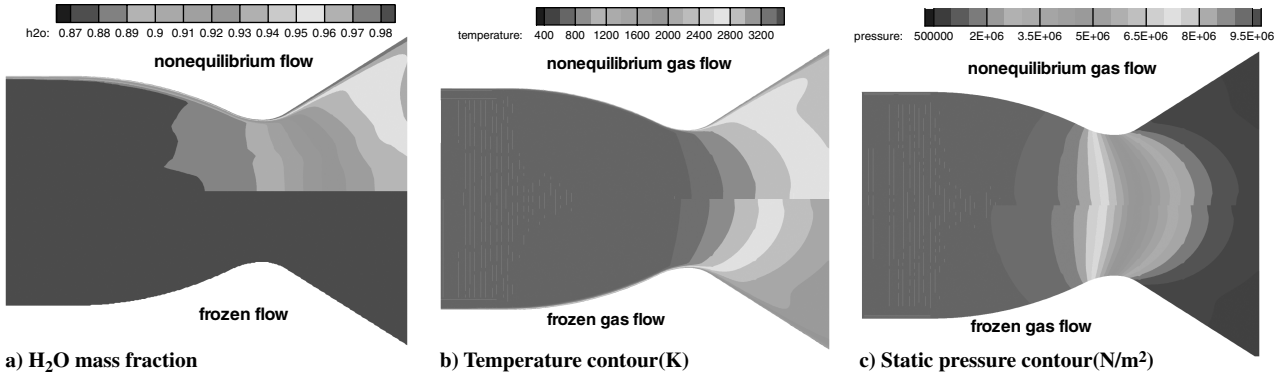

a) H_2O mass fraction **b) Temperature contour(K)** **c) Static pressure contour(N/m²)**

Fig. 14 Comparison of nonequilibrium/frozen hot-gas flowfield.

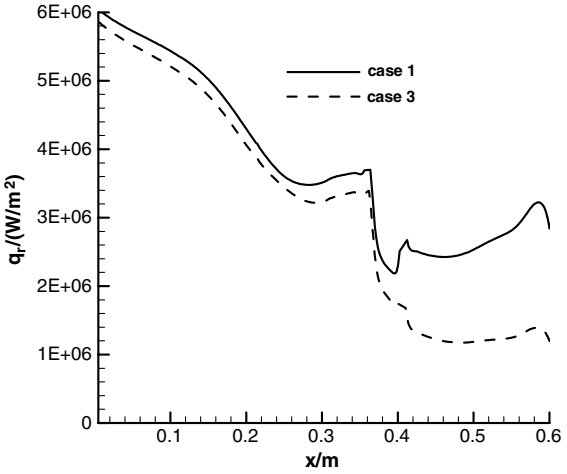

Fig. 15 Comparison of radiative wall heat fluxes.

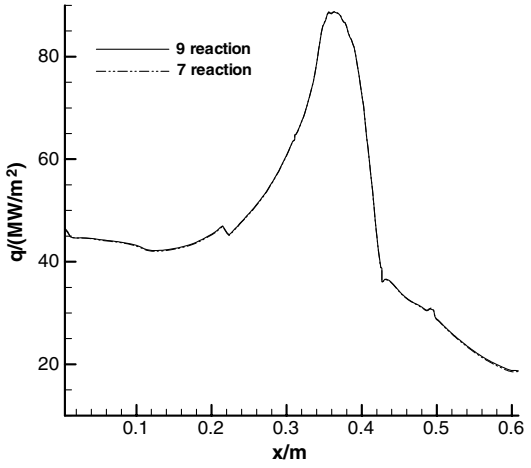

Fig. 16 Comparison of total wall flux.

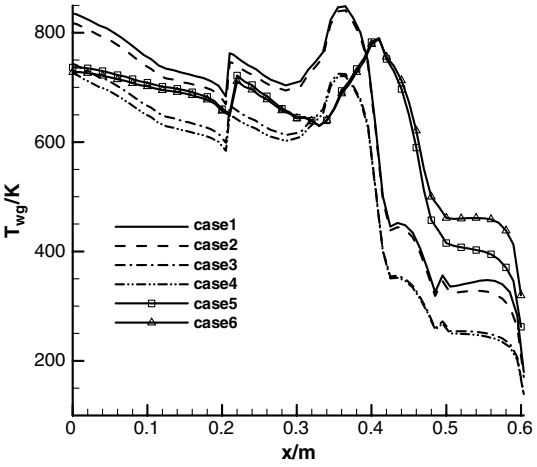

Fig. 18 Comparison of wall temperature.

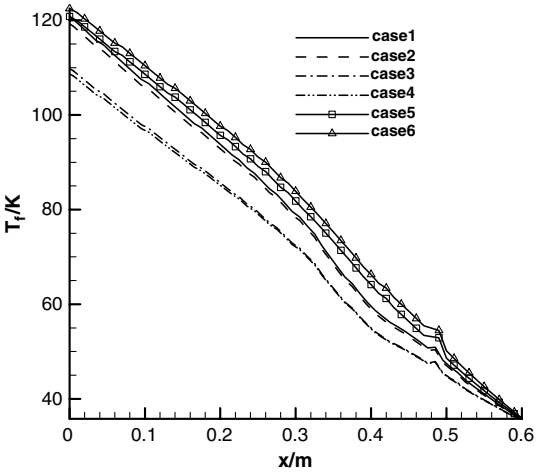

Fig. 19 Comparison of coolant temperature.

significant sharp reduction of wall heat flux. The hot-gas flow and heat transfer using CFD can capture this flow features reasonably well, while empirical equations can not capture it.

Figure 18 shows that the wall temperature distribution behave the same trend as wall heat flux. It can be seen from Fig. 18 that the location deviation of maximum hot-gas-side wall temperature of the two methodologies is obvious. In flows through a curved cooling channel, the interaction of pressure, viscous and inertial forces leads to a secondary motion described in the literature as Dean vortices [25]. The coolant mass flux redistribution caused by Dean vortices will enhance heat transfer in concave cooling channel (throat region) and deteriorate heat transfer in convex cooling channel (the convergent part of thrust chamber), so the maximum temperature should occur upstream of the throat, where the curvature is convex, that is to say the second methodology can capture this important flow feature. At the thruster inlet, hot-gas-side wall temperature is almost the same as its maximum value. This is because the inlet total temperature is assumed to be equal to combustion chamber total

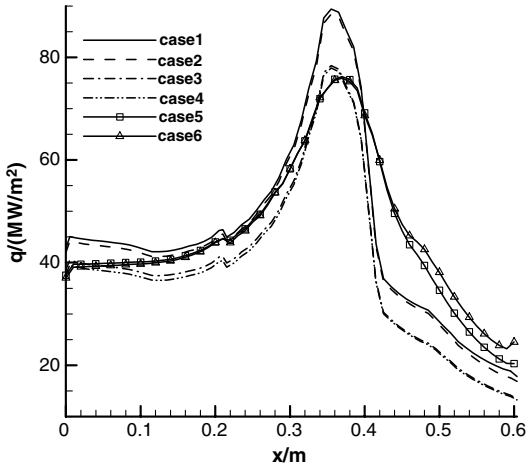

Fig. 17 Comparison of total wall heat flux.

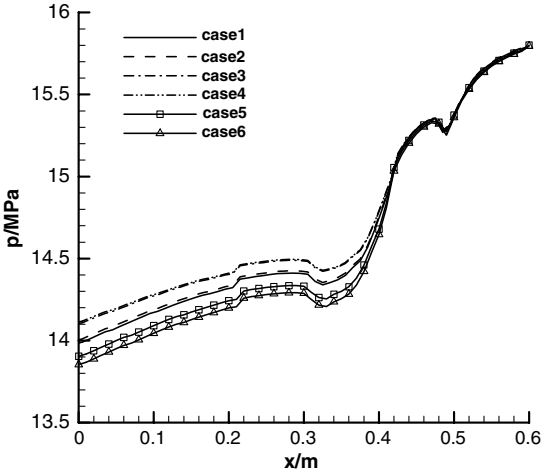

Fig. 20 Comparison of coolant pressure.

Table 6 Simulated results using four different methods

Method	Case 1	Case 2	Case 3	Case 4	Case 5	Case 6
Throat wall temperature	848.2 K	841 K	725 K	720 K	790 K	788 K
Throat wall heat flux	89.4 MW/m^2	88.45 MW/m^2	78.4 MW/m^2	77.9 MW/m^2	76.23 MW/m^2	75.92 MW/m^2
Pressure Drop						
Numerical	1.92 MPa	1.9 MPa	1.8 MPa	1.79 MPa	2.05 MPa	2 MPa
Experimental	2.2 MPa	2.2 MPa	2.2 MPa	2.2 MPa	2.2 MPa	2.2 MPa
Percent error	−12.7%	−13.6%	−18.2%	−18.6%	−6.8%	−9.1%
Temperature Rise						
Numerical	86.17	84.7	75.2	74.1	86.2	87.8
Experimental	85	85	85	85	85	85
Percent error	1.4%	−0.4%	−11.5%	−12.8%	1.41%	3.3%

temperature, which leads to the inlet gas temperature being much higher than the actual situation. Further improvements of simulation are expected to consider the atomization process of LOX jets emerged from injector elements and the flames from injector elements. The cooling channel occurs sudden expansion at axial location of 0.49 m and sudden contraction at axial location of 0.21 m, there are vortices in the cooling channel at those two locations due to inertia of coolant and sharp change in cooling channel geometry. The vortices intensify friction and strike among fluid elements will strengthen the mixing of the coolant and enhance the coolant heat transfer, so the hot-gas-side wall temperature is low and the axial temperature gradient is large at those two locations, which is harmful to the integrity of thrust chamber.

Figure 19 shows the bulk coolant temperature distribution for all cases. The coolant temperature increases continuously along the flow direction because the coolant absorbs heat transferred from the hot gas. The slope of temperature variation along the axial direction is an indication of the amount of heat absorbed by the coolant. The slope is almost constant, except for a small portion upstream of throat, where the heat flux is the largest.

Figure 20 shows the bulk coolant static pressure distribution for all cases. The heat transfer from the hot gas, as well as the cooling channel influences the coolant pressure. As shown in this figure, the pressure drop is larger in the throat region than the combustion chamber and nozzle exit. This is due to the reduced cooling channel width at the throat. Further improvements of simulation are expected to include the cooling channel inlet manifold and outlet annulus models to computational domain, which will cause large local pressure loss.

Table 6 is simulation results for all cases, the experimental pressure drop and temperature rise between inlet manifold and outlet annulus are 2.2 MPa and 85 K (experimental data supplied by Beijing Aerospace Propulsion Institute, CASC), respectively.

It seems that results of case 5 and case 6 fit better with experimental results as far as pressure drop and temperature rise are concerned. The empirical equations for hot-gas heat transfer assuming the frozen chemistry and all variables are uniform along the radial direction, it is a undesirable assumption as Fig. 14 shows, however, empirical equations can predict the variables of interest in a fast way. Besides the undesirable assumption, a huge database was necessary to adapted semi-empirical factors to individual propellant characteristics. Nevertheless it remained difficult to consider the boundary layer, finite-rate chemistry, and thermodynamics of hot gas which can be considered in the second methodology.

The results obtained using hot-gas frozen flow are lower than experimental results, that is to say it is not appropriate to execute the numerical simulation assuming frozen chemistry. From the table, we can see that radiation coupling in the simulation process can improve the prediction accuracy. The predicted coolant bulk temperature rise of case 1 is larger than experimental value. As noticed already, in a length downstream of thruster inlet, the predicted hot-gas-side wall flux of case 1 is larger than actual situation which will cause the larger computational coolant bulk temperature rise. It ought to include the atomization process of LOX jets emerged from injector elements and the flames from injector elements in the numerical procedure, in such a way, the calculated hot-gas-side wall heat flux will be lower in a length downstream of thruster inlet, and the calculated coolant bulk temperature rise should be lower than current value and fit better with experimental data. The predicted pressure drop of case 1 is smaller than experimental value. The cooling channel geometry changes at cooling channel inlet manifold and outlet annulus, i.e., sudden expansion/contraction and curvature effects. As coolant flows through sudden expansion/contraction cooling channel, there are large local pressure loss for the strike, friction of fluid element and collision with walls, the curving contour will also cause local pressure loss. It ought to include cooling channel inlet manifold and outlet annulus in the computational domain, in such a way, the calculated pressure drop of case 1 will be larger than current value and fit better with experimental data.

VI. Conclusions

Two computational methodologies with real gas thermophysical properties model were presented for liquid rocket engine thrust chamber regenerative cooling flow and heat transfer analysis. One methodology was coupled heat transfer between cooling channel and coolant using empirical equations to simulate the hot-gas-side heat transfer, the other methodology was coupled heat transfer among hot gas, cooling channel, coolant. Under the computational framework of this study, the following conclusions could be reached:

1) The second methodology with finite-rate chemistry and DO radiation model adopted in this study can be an effective method for predicting the flow and heat transfer in regeneratively-cooled thrust chamber; for higher accuracy, it ought to include the atomization process of LOX jets emerged from injector elements, the flames from injector elements in numerical procedure and cooling channel inlet manifold, outlet annulus in computational domain.

2) The hot-gas flows in thrust chamber with chemical reaction, in the combustion chamber and the convergent region of nozzle, the nonequilibrium effect is not so obvious, while in the divergent region of nozzle, the nonequilibrium effect is obvious which cause the radiative heat flux increases for much more H_2O participate in the radiation; various reduced reaction mechanisms have little influence on hot-gas heat transfer.

3) The location of maximum hot-gas-side wall flux and temperature occurs upstream of the throat; at sudden expansion/contraction location of cooling channel, the hot-gas-side wall temperature is low and the axial temperature gradient is large; in order to ensure integrity of thrust chamber, much more emphasis should put on those regions.

References

[1] Wennerberg, J. C., Anderson, W. E., Haberlen, P. A., Jung, H., and Merkle, C. L., "Supercritical Flows in High Aspect Ratio Cooling Channels," AIAA Paper 2005-4302.

[2] Preclik, D., Wiedmann, D., Oechslein, W., and Kretschmer, J., "Cryogenic Rocket Calorimeter Chamber Experiments and Heat Transfer Simulations," AIAA Paper 98-3440.

[3] Frohlich, A., Popp, M., Schmidt, G., and Thelemann, D., "Heat Transfer Characteristics of H_2/O_2: Combustion Chambers," AIAA Paper 93-1826.

[4] Marchi, C. H., Laroca, F., Silva, A. F., and Hinckel, J. N., "Numerical

Solutions of Flows in Rocket Engines with Regenerative Cooling," *Numerical Heat Transfer, A: Applications*, Vol. 45, No. 7, 2004, pp. 699–717.

[5] Kirchberger, C., Wagner, R., Kau, H., Soller, S., Martin, P., Bouchez, M., and Bonzom, C., "Prediction and Analysis of Heat Transfer in Small Rocket Chambers," AIAA Paper 2008-1260.

[6] Wang, T. S., and Luong, V., "Hot-Gas-Side and Coolant-Side Heat Transfer in Liquid Rocket Engine Combustors," *Journal of Thermophysics and Heat Transfer*, Vol. 8, No. 3, 1994, pp. 524–530.

[7] Liu, Q., Luke, E., Cinnella, P., and Tang, L., "Coupling Heat Transfer and Fluid Flow Solvers for Multi-Disciplinary Simulations," AIAA Paper 2004-996.

[8] Naraghi, M. H., Coats, D., and Dunn, S., "A Model for Design and Analysis of Regeneratively Cooled Rocket Engines," AIAA Paper 2004-3852.

[9] Naraghi, M. H., and Jokhakar, J., "A CFD-RTE Model for Thermal Analysis of Regeneratively Cooled Rocket Engines," AIAA Paper 2008-4557.

[10] Negishi, H., Kumakawa, A., Yamanishi, N., and Kurosu, A., "Heat Transfer Simulations in Liquid Rocket Engine Subscale Thrust Chambers," AIAA Paper 2008-5241.

[11] Negishi, H., Kumakawa, A., Moriya, S., Yamanishi, N., and Sunakawa, H., "Numerical Investigations of Heat Transfer Enhancement in a Thrust Chamber with Hot Gas Side Wall Ribs," AIAA Paper 2009-830.

[12] Shang, H. M., Chen, Y. s., and Liaw, P., "Investigation of Chemical Kinetics Integration Algorithms for Reacting Flows," AIAA Paper 95-0806.

[13] Yu Qi-Zheng, "The Basis of Radiative Heat Transfer," Higher Education Press, Beijing, 1996.

[14] Bartz, D. R., "A Simple Equation for Rapid Estimation of Rocket Nozzle Convective Heat Transfer Coefficients," *Jet Propulsion*, Vol. 27, No. 1, 1957, pp. 49–51.

[15] Schmidt, G., "Technik der Flüssigkeits-Raketentriebwerk," Daimler Chrysler Aerospace, Munich, 1999.

[16] Kang, Y.-D., Sun, B., GAO Xiang-yu, "Numerical Investigations of Thermal Stratification in Cooling Channel of Liquid Rocket Engine Thrust Chamber," *Journal of Aerospace Power*, Vol. 24, No. 8, 2009, pp. 1904–1910.

[17] Gordon, s., and McBride, B. J., "Computer Program for Calculation of Complex Chemical Equilibrium Compositions and Applications," NASA RP-1311, 1994.

[18] Shope, F. L., "Conjugate Conduction-Convection Heat Transfer with a High-Speed Boundary Layer," *Journal of Thermophysics and Heat Transfer*, Vol. 8, No. 2, 1994, pp. 275–281.

[19] Engblom, W., and Fletcher, B., "Validation of Conjugate Heat-Transfer Capability for Water-Cooled High-Speed Flows," AIAA Paper 2007-4392.

[20] Engblom, W., Fletcher, B., and Georgiadis, N., "Conjugate Conduction-Convection Heat-Transfer for Water-Cooled High-Speed Flows," AIAA Paper 2008-4653.

[21] Sagnier, P., and Marraffa, L., "Parametric Study of Thermal and Chemical Nonequilibrium Nozzle Flow," AIAA Paper 89-1856.

[22] Kacynski, K. K., "Thermal Stratification Potential in Rocket Engine Cooling Channels," NASA TM-4378, 1992.

[23] Woschnak, A., Suslov, D., and schwald, M. O., "Experimental and Numerical Investigations of Thermal Stratification Effects," AIAA Paper 2003-4615.

[24] Lemmon, E. W., Mclinden, M. O., and Friend, D. G., *Thermophysical Properties of Fluid Systems. NIST Chemistry WebBook*, NIST Standard Reference Database Number 69, NIST, Gaithersburg, MD, 2005.

[25] Sturgis, J., and Mudawar, F., "Single-Phase Heat Transfer Enhancement in a Curved, Rectangular Channel Subjected to Concave Heating," *International Journal of Heat and Mass Transfer*, Vol. 42, No. 7, 1999, pp. 1255–1272.